

## Ligand Design for Securing Ferromagnetic Exchange Coupling in Multimetallic Complexes

Scott W. Gordon-Wylie, Emile L. Bominaar, Terrence J. Collins,\* José M. Workman, Brian L. Claus, Robert E. Patterson, Stacy A. Williams, Brenda J. Conklin, Gordon T. Yee,\* and Susan T. Weintraub

**Abstract:** An approach is suggested for using ligands to control exchange coupling in multinuclear ions. The idea arose from structural, EPR, and magnetic studies of  $[\text{PPh}_4]_3\mathbf{3}$  (Scheme 1). Ferromagnetic coupling has been found between the  $\text{Co}^{\text{II}}$  and each  $\text{Co}^{\text{III}}$  in  $\mathbf{3}$  with  $J = -22 \pm 5 \text{ cm}^{-1}$  ( $J\mathbf{S}_1 \cdot \mathbf{S}_2$ ). It is suggested that dominant antiferromagnetic superexchange is absent because of the strong  $\sigma$ -donor capacity of the tetradentate ligand

$[\kappa^4\text{-PAC}^*]^{4-}$  (Fig. 1). The ligand interacts at  $\text{Co}^{\text{III}}$  primarily with a single d orbital; it is thus best able to participate in superexchange. The interaction makes the unique

d orbital strongly  $\sigma$ -antibonding and empty for each  $d^6$ ,  $S = 1$ ,  $\text{Co}^{\text{III}}$  ion in  $\mathbf{3}$ , that is, unavailable for antiferromagnetic coupling, but available for ferromagnetic pathways by a Goodenough–Kanamori mechanism. By corollary, when any  $[\kappa^4\text{-PAC}^*]^{4-}$ -type ligand with any magnetic ion  $M_a$  in the tetradentate site binds any magnetic ion  $M_b$  in the bidentate site, ferromagnetic coupling should be favored provided  $M_a$  is not a  $d^9$  ion.

**Keywords**  
exchange coupling · ferromagnetic properties · ligand design · magnetic properties · multimetallic complexes

### Introduction

The study of magnetic behavior in multimetallic complexes is a growing field with a distinguished history.<sup>[1–12]</sup> Theoretical treatments have included molecular orbital and valence bond approaches,<sup>[4, 13–16]</sup> providing a basis for design principles that have been used to predict the sign of the exchange interactions in real or conceivable multinuclear ions.<sup>[8, 12]</sup> The most useful principle derives from the orthogonality or nonorthogonality of orbitals with unpaired spins on different sites. Ferromagnetic coupling arises when unpaired electrons on different ions reside in magnetic orbitals<sup>[1, 7]</sup> that are mutually orthogonal, whereas antiferromagnetic coupling results when the unpaired electrons reside in nonorthogonal magnetic orbitals. Kahn and others<sup>[18, 19]</sup> have succeeded in assembling multimetallic ions with exchange coupling of predetermined sign in a two-step design process. First, a ligand system is prepared that accommodates two or more magnetic ions in specific locations. Second, the metal ions are selected such that the magnetic orbitals are arranged to have orthogonal or nonorthogonal juxtapositions.

In this contribution, we suggest a ligand-based method for eliminating the strongest antiferromagnetic exchange pathway in designed multinuclear ions and favoring a ferromagnetic pathway in its stead. The approach is based on the hypotheses of Goodenough that overlap of a half-filled orbital on one ion with either an empty or a filled orbital on another gives rise to a ferromagnetic interaction.<sup>[20]</sup> The method arises from the ability, through design of ligand bonding properties, to considerably raise the energy of a single d orbital at one magnetic ion; when the first metal interacts with a second magnetic ion, this d orbital is uniquely important for superexchange. The method can be summarized as follows: A ligand system ( $[\kappa^4\text{-PAC}^*]^{4-}$ , Fig. 1) is chosen in which four strongly donating amide and alkoxide groups present an unusually strong planar  $\sigma$  field. In complex  $\mathbf{1}$ , the ligand system interacts much more strongly with one d orbital ( $d_{xz}$  in the molecular  $C_{2v}$  symmetry) of the  $M_a$  ion than with the other four. This orbital becomes strongly  $\sigma$ -antibonding such that it is empty for any  $M_a$  ion other than a  $d^9$  ion. The spin states and redox potentials found for numerous first-row complexes indicate  $[\kappa^4\text{-PAC}^*]^{4-}$  and related strongly donating planar tetradentate ligands isolate one d orbital at high energy.<sup>[21]</sup> Moreover, the pronounced destabilization of just

\*] Prof. T. J. Collins, S. W. Gordon-Wylie, E. L. Bominaar, J. M. Workman, B. L. Claus, R. E. Patterson, S. A. Williams  
Department of Chemistry, Carnegie Mellon University  
4400 Fifth Avenue, Pittsburgh, PA 15213 (USA)  
Telefax: Int. code + (412) 268-1061  
Prof. G. T. Yee, B. J. Conklin  
Department of Chemistry, University of Colorado at Boulder  
Campus Box 215, Boulder, Colorado 80309 (USA)  
Prof. S. T. Weintraub  
University of Texas Health Science Center at San Antonio

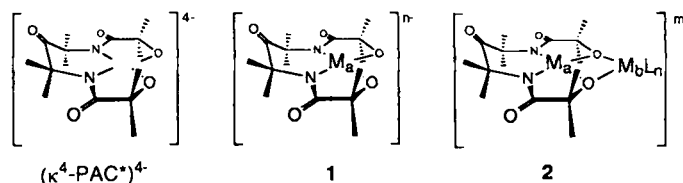
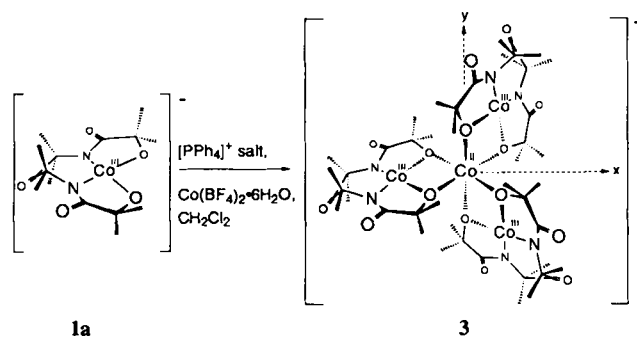


Fig. 1. Structures of fundamental complexes.

one d orbital appears also to hold for five- and six-coordinate complexes of  $[\kappa^4\text{-PAC}^*]^{4-}$ -type chelates with added axial ligands.<sup>[21]</sup> Complex **1** can coordinate a second magnetic ion,  $M_b$ , to give complexes of type **2**, thereby allowing for exchange interactions to be studied (Fig. 1). Because the highest-lying d orbital of **1** (for  $d^x$ ,  $x < 9$ ) is empty, it is not available for an antiferromagnetic interaction with  $M_b$  in **2**. On the other hand, it is available for promoting a ferromagnetic interaction. While there can be many exchange pathways for two magnetic ions with two bridging atoms in the planar conformation of Figure 1, the orbitals associated with the very strong  $M_a$ -ligand  $\sigma$ -bonding are likely to be the important ones for ligand-mediated exchange. Since all molecular orbitals derived from the uniquely destabilized  $M_a$  d orbital cannot be part of an antiferromagnetic pathway in **2**, because they are either empty (antibonding) or filled (bonding), ferromagnetic exchange coupling between  $M_a$  and  $M_b$  is likely to result. Moreover,  $M_b$  can be chosen to ensure that overlap occurs between one of its magnetic orbitals and the high-lying  $M_a$  orbital to enhance ferromagnetic exchange.

The suggestion of this ligand-based design method for controlling the sign of magnetic exchange coupling arises from an analysis of the exchange coupling within the tetranuclear anion in  $[\text{PPh}_4]_3$  (Scheme 1). The remainder of the report is organized



Scheme 1. Synthesis of  $[\text{PPh}_4]_3$ .

as follows: First, the synthesis, characterization, and structural properties of the multimetallic ion are presented, and the electronic structures of the interacting ions are discussed. Second, the EPR and bulk magnetic studies of the spin system are summarized, and the theory employed to fit the data is briefly described. Third, the interpretation relating the findings of the magnetic study to the known chemical and electronic properties of the constituent  $\text{Co}^{\text{III}}$  and  $\text{Co}^{\text{II}}$  ions is further discussed.

## Results and Discussion

**Structural Properties of  $[\text{PPh}_4]_3$ :** Three equivalents of **1a** bind to  $\text{Co}^{\text{II}}$  to give the tetranuclear ion **3** (Scheme 1). The crystal structure of the  $[\text{PPh}_4]^+$  salt has been solved (Fig. 2). The system is well configured to support exchange coupling only between the central  $\text{Co}^{\text{II}}$  ion and the three surrounding symmetry-related  $\text{Co}^{\text{III}}$  ions. The average distance between  $\text{Co}^{\text{III}}$  and  $\text{Co}^{\text{II}}$  is 3.06 Å with the oxygen bridges providing a potential superexchange pathway. The average  $\text{Co}^{\text{III}} \cdots \text{Co}^{\text{III}}$  distance is 5.30 Å: there are no direct pathways for  $\text{Co}^{\text{III}}\text{-Co}^{\text{III}}$  exchange coupling. Intermolecular  $\text{Co} \cdots \text{Co}$  distances are considerably greater with the shortest being 8.20 Å: interionic magnetic interactions should be small.  $D_3$  symmetry extends well over the entire **3** anion, which can be viewed as a three-bladed propeller with the blades

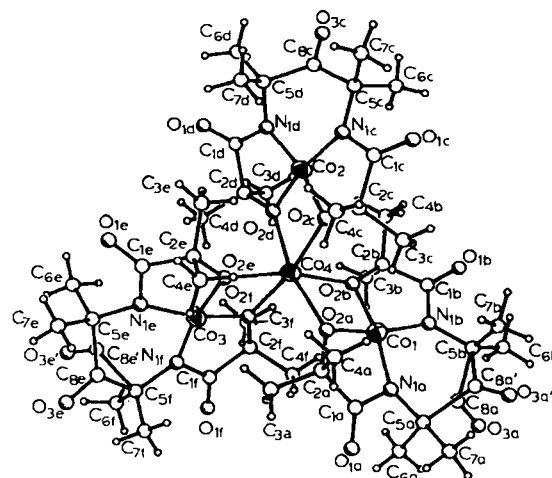


Fig. 2. Molecular structure of **3**: ORTEP drawing with nonhydrogen atoms drawn to encompass 50% of electron density. Selected bond lengths (Å): Co4-O2a, 2.134(7); Co4-O2b, 2.125(7); Co4-O2c, 2.159(6); Co4-O2d, 2.138(7); Co4-O2e, 2.146(7); Co4-O2f, 2.136(7); Co1-N1a, 1.824(9); Co1-N1b, 1.836(8); Co2-N1c, 1.828(8); Co1-O2a, 1.810(7); Co1-O2b, 1.820(7); Co2-O2c, 1.813(7); Co2-O2d, 1.826(6); Co3-O2e, 1.823(6); Co3-O2f, 1.823(7); Co2-N1d, 1.806(8); Co3-N1e, 1.838(9); Co3-N1f, 1.820(8). Selected bond angles (°): Co1-O2a-Co4, 100.9(3); Co1-O2b-Co4, 101.0(3); Co2-O2c-Co4, 100.4(3); O2a-Co4-O2b, 71.5(3); O2a-Co4-O2c, 98.0(3); O2a-Co4-O2d, 166.2(3); O2a-Co4-O2e, 99.1(3); O2a-Co4-O2f, 91.1(3); O2b-Co4-O2c, 89.6(3); O2b-Co4-O2d, 98.9(3); O2b-Co4-O2e, 167.0(3); O2b-Co4-O2f, 99.3(3); O2c-Co4-O2d, 71.5(2); O2c-Co4-O2e, 100.8(3); O2c-Co4-O2f, 168.9(3); O2d-Co4-O2e, 91.8(3); O2d-Co4-O2f, 100.4(2); O2e-Co4-O2f, 71.4(2); O2a-Co1-O2b, 86.6(3); O2a-Co1-N1a, 88.1(4); Co2-O2d-Co4, 100.8(3); Co3-O2e-Co4, 110.8(3); Co3-O2f-Co4, 101.2(3); O2a-Co1-N1b, 167.6(4); O2b-Co1-N1a, 167.4(4); O2b-Co1-N1b, 88.4(3); N1a-Co1-N1b, 99.0(4); O2c-Co2-O2d, 87.2(3); O2c-Co2-N1c, 87.6(3); O2c-Co2-N1d, 166.1(3); O2d-Co2-N1c, 168.2(4); O2d-Co2-N1d, 88.6(3); N1c-Co2-N1d, 98.8(4); O2e-Co3-O2f, 86.5(3); O2e-Co3-N1e, 88.4(4); O2e-Co3-N1f, 167.8(4); O2f-Co3-N1e, 168.3(4); O2f-Co3-N1f, 88.6(3); N1e-Co3-N1f, 98.4(4). Nonbonded distances (no standard deviations): Co4-Co1, 3.049; Co4-Co2, 3.060; Co4-Co3, 3.067; O2a-O2b, 2.489; O2c-O2d, 2.510; O2e-O2f, 2.499; O2a-O2c, 3.240; O2a-O2e, 3.257; O2a-O2f, 3.048; O2b-O2c, 3.019; O2b-O2d, 3.239; O2b-O2f, 3.247; O2c-O2e, 3.318; O2d-O2e, 3.076; O2d-O2f, 3.284.

defined by the mean **1a** planes (Fig. 3). It is important to note for the analysis of the exchange coupling that the angles define an octahedron at  $\text{Co}^{\text{II}}$  that has been squashed along a three-fold axis. The O-Co-O angles at the central  $\text{Co}^{\text{II}}$  are all 71° and at each  $\text{Co}^{\text{III}}$  are all 87°. The  $\text{Co}^{\text{III}}\text{-O-Co}^{\text{II}}$  angles lie in the range of 100–101°. The local coordination environment at the  $\text{Co}^{\text{III}}$  and  $\text{Co}^{\text{II}}$  ions will be analyzed next to determine how best to consider the local magnetic centers in the theoretical treatment of the magnetic properties.

First, the  $\text{Co}^{\text{III}}$  monomer, **1a**, is considered. The unusual planar four-coordinate structure has been attributed to the strong  $\sigma$ -donor capacity of  $[\kappa^4\text{-PAC}^*]^{4-}$ ,<sup>[22]</sup> which is expected from the high  $pK_a$  values of the secondary amido (ca. 18)<sup>[23]</sup> and alkoxido ligands (ca. 17).<sup>[24]</sup> This  $\sigma$ -donor capacity of  $[\kappa^4\text{-PAC}^*]^{4-}$  also explains some unusual properties of other related first-row transition-metal complexes. For example, in the  $d^9$   $\text{Cu}^{\text{II}}$  complex  $[\text{Cu}(\kappa^4\text{-PAC}^*)]^{2-}$ , the  $\text{Cu}^{\text{II/III}}$  couple is found at  $-0.60$  V (vs. SCE,  $\text{CH}_2\text{Cl}_2$ ):  $\text{Cu}^{\text{II/III}}$  couples are usually found at potentials greater than 1 V.<sup>[25]</sup> The exceptionally negative  $\text{Cu}^{\text{II/III}}$  couple implies that the magnetic HOMO of  $[\text{Cu}^{\text{II}}(\kappa^4\text{-PAC}^*)]^{2-}$  is unusually high in energy. Similarly, tetradentate tetraamido  $N$ -ligands closely related to  $[\kappa^4\text{-PAC}^*]^{4-}$  stabilize low-spin, planar, four-coordinate  $\text{Ni}^{\text{III}}$  ( $d^7$ ,  $S = 1/2$ ),<sup>[26]</sup> the only homogeneous high-spin  $\text{Fe}^{\text{IV}}$  complex ( $d^4$ ,  $S = 2$ ),<sup>[27]</sup> and the relatively uncommon intermediate spin state for  $\text{Fe}^{\text{III}}$  ( $d^5$ ,  $S = 3/2$ ).<sup>[27]</sup>

In each case, the chelate's strong  $\sigma$ -donor capacity results in one d orbital being raised high enough in energy that the spin

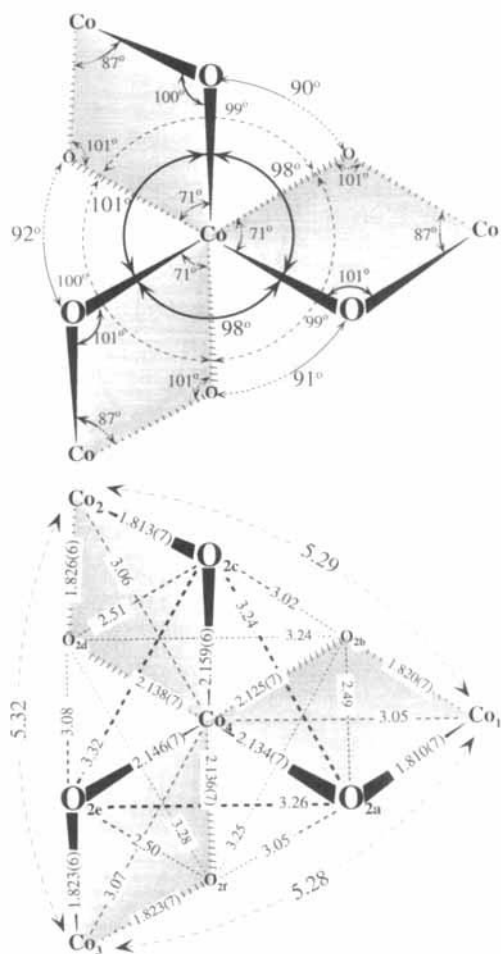


Fig. 3. Structure of **3** showing the  $D_{3h}$  symmetry, bond angles, and bond lengths of the molecular propeller.

state corresponds to the maximum multiplicity attainable by distribution of the metal electrons among the four remaining d orbitals. This orbital energy isolation is illustrated in Figure 4 for  $C_{2v}$  planar  $\text{Co}^{\text{III}}$ , where the  $\sigma$ -only bonding orbitals of the four donors transform as  $2A_1 + 2B_1$ , and the Co d orbitals transform as  $2A_1, A_2, B_1$ , and  $B_2$ . The  $\sigma$ -antibonding  $B_1$  orbital ( $d_{xz}$ )<sup>[28]</sup> points directly at the ligands: one can assume it is well-separated in energy from the other four d orbitals, giving rise to the observed  $S = 1$  ground state.<sup>[22, 29, 30]</sup> The two  $\text{Co}^{\text{III}}$   $A_1$  orbitals are oriented to have lesser interactions with the ligand system than  $B_1$ ; they are likely to be the magnetic orbitals. The  $A_2$  and  $B_2$  metal orbitals have no  $\sigma$  interactions with the ligands.

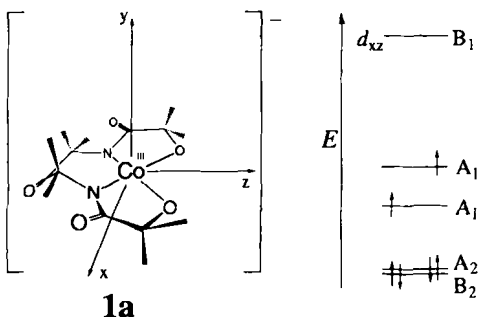


Fig. 4.  $C_{2v}$  symmetry of **1a** showing estimated ordering of frontier molecular orbitals.

Coordination of **1a** to a second metal ion should reduce the donor capacity of  $[\kappa^4\text{-PAC}^*]^{4-}$  to the  $\text{Co}^{\text{III}}$  ion and, consequently, the splitting between the  $B_1$  orbital and the other d orbitals. However, modification of the molecular structure of **1a** (and by implication the electronic structure) is small, because binding to the  $\text{Co}^{\text{II}}$  ion is weak (see below). As in **1a**, deviations from the mean planes formed by each  $\text{Co}^{\text{III}}$  and the two N and O donor atoms range from 0.13 to 0.15 Å for **3**. The close relationship between free and coordinated **1a** is emphasized by the similarity of the average  $\text{Co}^{\text{III}}\text{-O}$  (1.819(16) Å) and  $\text{Co}^{\text{III}}\text{-N}$  (1.83(2) Å) bond lengths to the values found in the parent monomer ( $\text{Co-O}_{\text{av}}$ , 1.794(1) Å;  $\text{Co-N}_{\text{av}}$ , 1.862(3) Å);<sup>[22]</sup> these distances are also similar to those found in related mononuclear ions ( $\text{Co-O}_{\text{av}}$ , 1.808(11) Å;  $\text{Co-N}_{\text{av}}$ , 1.84(2) Å).<sup>[29-32]</sup> Therefore, it is reasonable to assume the same local spin state ( $S = 1$ ) will be found in all these closely related ions. A variable-temperature SQUID magnetic study of  $[\text{PPh}_4]\text{1a}\cdot\text{CH}_2\text{Cl}_2$  can be fitted well with an axial  $S = 1$  model with an appreciable zero-field splitting,  $D = 37.3 \text{ cm}^{-1}$  (Fig. 5). These considerations lead us to conclude that each  $\text{Co}^{\text{III}}$  site contributes a local spin of  $S = 1$  to the total spin of the multimetallic complex.

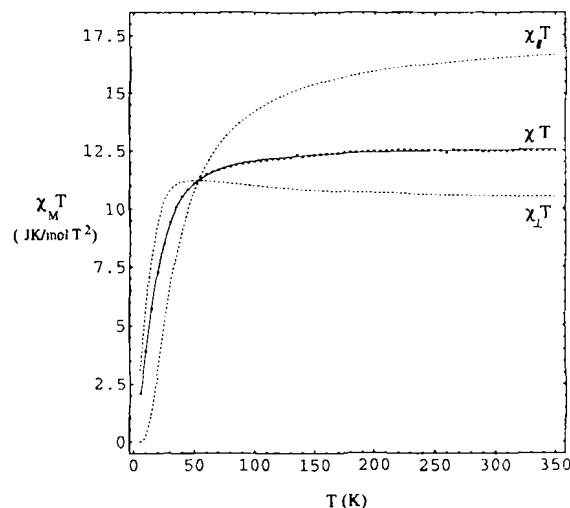


Fig. 5. Magnetic data for  $S = 1$   $[\text{PPh}_4]\text{1a}$  at 0.1 T. Data points ( $\cdot$ ) are corrected for diamagnetic contributions from the holder and from the complex by using Pascal constants and for temperature-independent paramagnetism. The fit ( $\mathcal{H} = D \left( S_z^2 - \frac{S(S+1)}{3} \right) + g\mu_B S \cdot \hat{H}$ , solid line) was evaluated with the parameters  $g_{\perp} = 2.03$ ,  $g_{\parallel} = 2.65$ , and  $D = 37.3 \text{ cm}^{-1}$  obtained by least-squares fitting of the data ( $R = 1.27 \times 10^{-5}$ ).

Consideration is given to the central  $\text{Co}^{\text{II}}$  magnetic ion in the section on the analysis of the magnetic data because the  $\text{Co}^{\text{II}}$  ion presents the most difficult component of the theoretical analysis. Here, we point out several preparatory facts for the magnetic analysis. The long average  $\text{Co}^{\text{II}}\text{-O}$  bond length (2.140(17) Å) indicates that a weak-field description is appropriate ( $d^7$ , three unpaired electrons). The structural data reveal a trigonal distortion from the octahedral coordination at the central  $\text{Co}^{\text{II}}$  ion. A number of investigators have described such distortions by focusing primarily on the angle between the three-fold axis and the  $\text{Co}^{\text{II}}\text{-ligand}$  bonds.<sup>[33, 34]</sup> We have found it to be useful to treat the trigonometry of the distortion of **3** in the context of two angles: the  $\text{O-Co}^{\text{II}}\text{-O}$  angle and  $\alpha$ , the angle between the normals to the **1a** mean planes and the  $C_3$  axis (Fig. 6). When  $\alpha$  is  $0^\circ$ , the propeller blades lie in a plane perpendicular to the  $C_3$  axis, a physically unrealistic situation. When  $\alpha$  is  $90^\circ$ , the blades lie parallel to and intersect at the  $C_3$  axis at the  $D_{3h}$  limit.<sup>[35]</sup> In **3**,

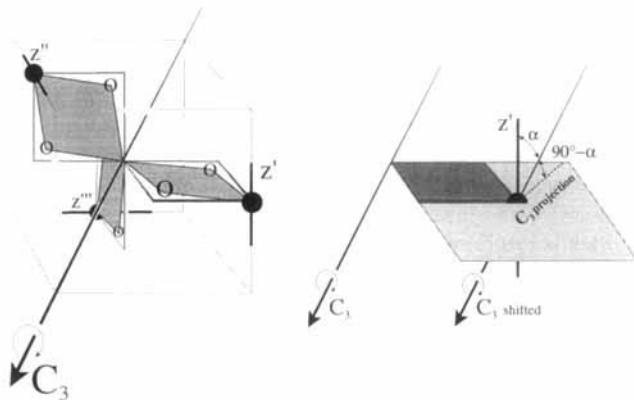


Fig. 6. Left: Schematic representation of the geometry of the tetranuclear complex showing the orthogonality of the "propeller blades" represented by the bridging O atoms and the Co<sup>III</sup> centers. Right: A representation of one propeller blade showing important angles.

the O–Co<sup>II</sup>–O angles (71°) are distorted from the octahedral value (90°), but the angle  $\alpha$  (54.2°) lies almost exactly at the magic angle (54.7°), such that the normals to the **1a** mean planes are orthogonal within experimental error (Fig. 6, left). This orthogonality has significant consequences for the analysis of the magnetic properties (see below).

The long Co<sup>II</sup>–O bonds hint that the Co<sup>II</sup> center should be labile in solution. Some key EPR experiments for the analysis of the spin system have been performed in the weakly coordinating solvent CH<sub>2</sub>Cl<sub>2</sub>. Thus, it was important to examine the dissociation behavior of **3** in CH<sub>2</sub>Cl<sub>2</sub>. Evidence is provided by <sup>1</sup>H NMR spectroscopy and by electrospray ionization mass spectrometry (ESIMS) that the tetranuclear structure is effectively maintained in dichloromethane solution in the EPR concentration range (0.42 mM) used for obtaining spin parameters at low temperature. At 22 °C, the <sup>1</sup>H NMR spectrum of [PPh<sub>4</sub>]**3** is concentration- and temperature-dependent. At concentrations of 3.3–19 mM, four singlets of equal integrated intensity are observed (Fig. 7); this is consistent with the tetrameric structure found in the solid state: the molecular C<sub>3</sub> and C<sub>2</sub> axes of the D<sub>3</sub> point group require the twenty-four methyl groups of **3** to

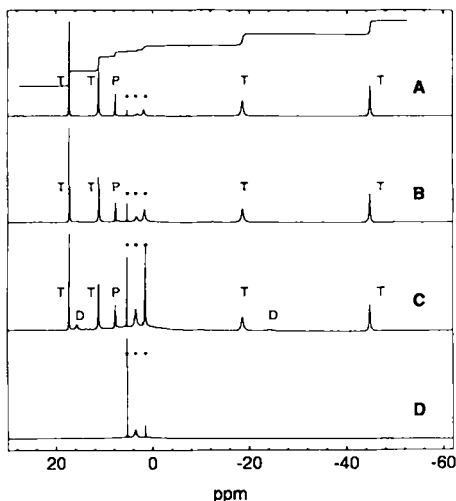


Fig. 7. <sup>1</sup>H NMR spectra of [PPh<sub>4</sub>]**3** in CD<sub>2</sub>Cl<sub>2</sub> at 22 °C and at different concentrations. A, 3.3 mM; B, 1.3 mM; C, 0.4 mM; D, CD<sub>2</sub>Cl<sub>2</sub>. T: signals of the tetranuclear ion. D: signals associated with dissociation of **3**. P: signals associated with [PPh<sub>4</sub>]<sup>+</sup> (partial diamagnetic suppression). \*: Signals arising from the solvent and from cavity water vapor.

behave as four inequivalent sets. As expected, the NMR signals are found in quite different positions from the parent Co<sup>III</sup> monomer.<sup>[22]</sup> As the 3.3 mM sample is diluted, additional signals appear in the spectrum, which we suggest arise from the dissociation of **1a** from **3**: the NMR spectrum of the 0.4 mM solution suggests a few percent dissociation under equilibrium conditions. The positions of the signals attributed to **3** do not shift on sample dilution; this suggests that the dissociation of **1a** from **3** is slow on the NMR time scale. The positions of the NMR signals vary with temperature in a manner that is independent of the dissociation equilibria: the signal of **3** at  $\delta = -46$  moves rapidly upfield as the temperature is lowered, while the remaining three signals move comparatively little. We are further studying this temperature-dependent behavior, which we attribute to magnetic effects within the tetranuclear ion. In the EPR spectrum at 4 K, **3** retains its axial nature and *g* values over the concentration range of 0.1–3.3 mM. This suggests that the dissociation equilibria in favor of **3** as the temperature is reduced. No other signals were observed in the EPR field window (0–10 kG, Fig. 9). The ESIMS of [PPh<sub>4</sub>]**3** in CH<sub>2</sub>Cl<sub>2</sub> also supports the NMR observation that **3** undergoes concentration-dependent dissociation at room temperature. Decreasing the concentration of a 0.4 mM ESIMS sample of [PPh<sub>4</sub>]**3** in CH<sub>2</sub>Cl<sub>2</sub> results in a change in the relative ion intensities for the two observable species, **3** and **1a**. At 0.4 mM concentration, the ion-intensity ratio **3**:**1a** is approximately 20:1, but this ratio decreases as the solution is diluted. At a [PPh<sub>4</sub>]**3** concentration of 4  $\mu$ M, the **3**:**1a** ion intensity ratio is approximately 3:1 (Fig. 8).

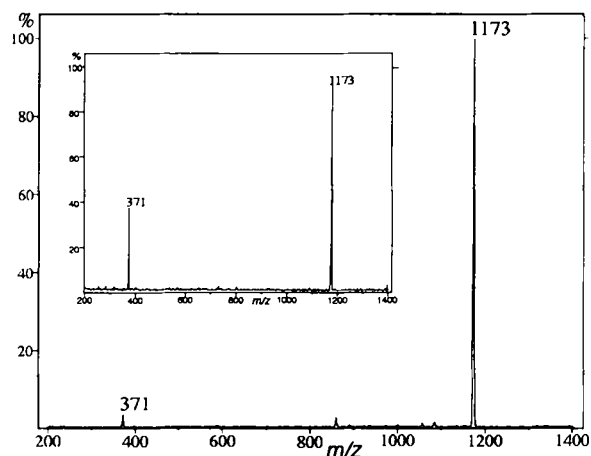


Fig. 8. Electrospray ionization mass spectrum of 0.4 mM [PPh<sub>4</sub>]**3** in CH<sub>2</sub>Cl<sub>2</sub>. Insert spectrum: 4  $\mu$ M [PPh<sub>4</sub>]**3** in CH<sub>2</sub>Cl<sub>2</sub>.

Although some slight variability was found when very dilute samples were subjected to repeated ESIMS analysis, more concentrated solutions showed no variability in the **3**:**1a** ion-intensity ratio. Thus, the body of data from NMR, EPR, and ESIMS studies consistently implies that the EPR parameters obtained at low temperature in CH<sub>2</sub>Cl<sub>2</sub> are those of essentially pure **3**.

**Determination of the exchange-coupling constant in **3**: Description of the model:** The EPR data for [PPh<sub>4</sub>]**3** (Fig. 9) in dilute frozen solution (0.42 mM, CH<sub>2</sub>Cl<sub>2</sub>, in the presence of 95  $\mu$ M [Cu(TPP)] as an independent internal temperature standard) indicates an approximately axial *g* tensor, which is consistent with the presence of a molecular threefold axis.<sup>[36]</sup> When the 4.2 K EPR spectrum is qualitatively fitted to an axial,<sup>[37]</sup> fictitious spin,  $S' = 1/2$  manifold, the calculated EPR *g* values are

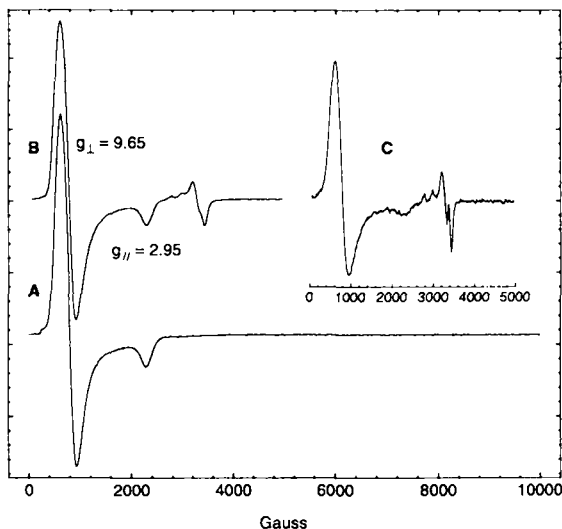


Fig. 9. EPR spectrum at 4.2 K of [PPh<sub>4</sub>]<sub>3</sub>. A: Spectrum from 0–10 kG, 1.3 mm. B: The effective *g* values are indicated and the resonances at 3200 G are from the [Cu<sup>II</sup>(TPP)] internal standard, 0.42 mm. C: Spectrum obtained at 18 K, 0.42 mm.

$g_{\perp} \approx 9.65$  and  $g_{\parallel} \approx 3.0$ . In Figure 10, a plot is presented of  $I_i T$  vs.  $T$ , where the intensity  $I_i$  is obtained by double integration of the derivative EPR signal. The value of the molecular zero-field splitting  $D_{\text{tet}}$  defined by the common effective operator [Eq. (1)], for describing the energy gaps between the Kramers

$$H_{\text{zfs}} = D_{\text{tet}} \left[ S_z^2 - \frac{33}{4} \right] \quad (1)$$

doublets of a spin  $S = 9/2$  multiplet, was estimated by fitting of the  $I_i T$  vs.  $T$  plot by using the expression (2) for the thermal occupation of the resonant ground doublet, in which  $D_{\text{tet}}$  and  $c$  are adjustable parameters. The fit results in the optimal

$$I_i T = c / (1 + e^{-2D_{\text{tet}}/kT} + e^{-6D_{\text{tet}}/kT} + e^{-20D_{\text{tet}}/kT}) \quad (2)$$

value for  $D_{\text{tet}}$  of  $14.2 \text{ cm}^{-1}$ , for which the simulated temperature-dependence is given in Figure 10 (Curve A).<sup>[37]</sup> We recognize that this treatment significantly underestimates the actual number of low-lying states, including resonant and non-

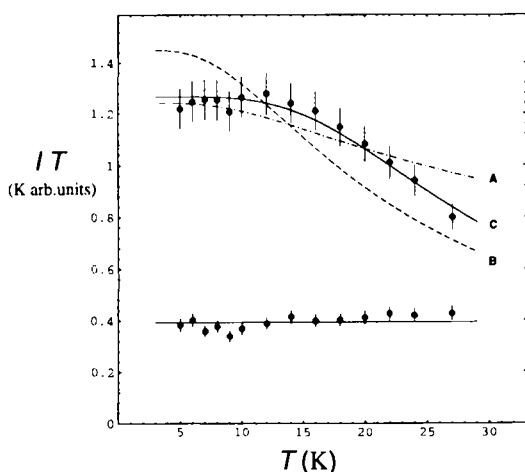


Fig. 10.  $I_i T$  vs.  $T$  plots for [PPh<sub>4</sub>]<sub>3</sub> (upper plots) and [Cu<sup>II</sup>(TPP)] (lower plot).  $I_i$  for [Cu<sup>II</sup>(TPP)] is scaled by a factor of 7.5. A: Fit based on Equation (2). B: Calculated by means of Equation (3) with the parameters of line 4 (Table 1). C: Fit based on Equation (8).

resonant states. We will return to fit the data of Figure 10 once the full model has been derived, allowing for the temperature-dependence of the populations of all low lying states to be included in the calculation; this will serve as a check for the model.

The main objective of the following analysis is the determination of the exchange-coupling constant  $J$  between the central Co<sup>II</sup> and each outer Co<sup>III</sup>. The mutual couplings of the non-bridged Co<sup>III</sup> ions are most likely small and will be ignored. The high-temperature data for the effective magnetic moment ( $\mu_{\text{eff}} \approx 8.5\text{--}9.7\mu_B$ ; Fig. 11) lie between the spin-only values

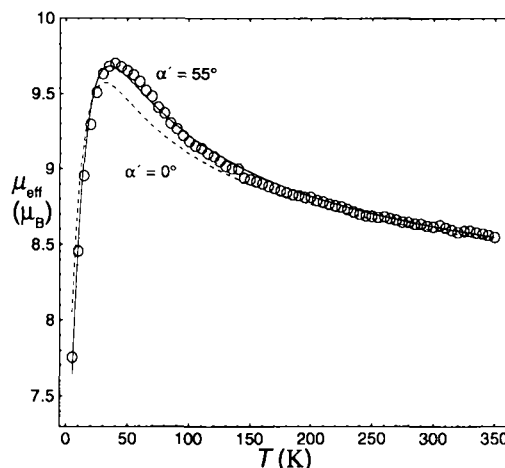


Fig. 11. Magnetic data for [PPh<sub>4</sub>]<sub>3</sub> recorded at 0.1 T. Data points (o) are corrected for diamagnetic contributions from the holder and nujol suspending agent and from the complex by using Pascal constants. The fit (solid line for  $\alpha' = 55^\circ$ ) is evaluated with the spin-Hamiltonian parameters [Eq. (3)] with  $\gamma = -5/4$ ,  $\nu = 225 \text{ cm}^{-1}$ , and  $\delta = 500 \text{ cm}^{-1}$  fixed, and  $D = 34.3 \text{ cm}^{-1}$ ,  $J_{\parallel} = J_{\perp} = -23.5 \text{ cm}^{-1}$ ,  $g_{\parallel} = 3.6$ , and  $g_{\perp} = 2.0$  obtained by least-squares fitting of the data. The  $\alpha' = 0^\circ$  curve is obtained for the same values of the spin-Hamiltonian parameters.

( $\mu_{\text{eff}} \approx 8\mu_B$  and  $\mu_{\text{eff}} \approx 10\mu_B$  for spins  $S = 7/2$  and  $S = 9/2$ , respectively) and imply a  $J$  value with a ferromagnetic sign. An antiferromagnetic exchange-coupling constant would yield a ground state with spin  $S = 3/2$ , which would have a much lower moment ( $\mu_{\text{eff}} \approx 3.9\mu_B$ ). The presence of only moderate exchange splittings is evident from the considerable reduction of  $\mu_{\text{eff}}$  at higher temperatures. The determination of the magnitude of  $J$  is an intricate matter, hampered by the fact that the exchange splittings are of the same order of magnitude as the zero-field splittings (see below). This fact prevents us from dealing with the problem in the coupled-spin representation. Spin is not a good quantum number for **3**: states of lower spin multiplicity are admixing into the ground state, which presents a second cause for the intermediate values observed for the effective magnetic moment.

Our analysis of the magnetic data of **3** (Fig. 11) is based on the threefold symmetric Hamiltonian shown in Equation (3),

$$H = \nu \vec{I} \cdot \vec{s}_4 + \delta \left( I_{4,z}^2 - \frac{2}{3} \right) + D [s_{1,z}^2 + s_{2,z}^2 + s_{3,z}^2 - 2] + \sum_{j=1,2,3} \vec{s}_4 \cdot \hat{J}_j \cdot \vec{s}_j + \mu_B \vec{H} \left[ \gamma \vec{I}_4 + 2 \vec{s}_4 + \sum_{j=1,2,3} \hat{g}_j \cdot \vec{s}_j \right] \quad (3)$$

where  $s_4 = 3/2$  and  $s_1 = s_2 = s_3 = 1$  are the spins of the Co<sup>II</sup> and the three Co<sup>III</sup> ions, respectively. With regard to the first term of Equation (3), the electronic ground state of the Co<sup>II</sup> derives from a  $^4T_1$  term in octahedral symmetry and can be described by an effective orbital momentum  $l = 1$ .<sup>[38, 39]</sup> The composition of

the  ${}^4T_1$  ground state [Eq. (4)] depends on the relative strength of

$$|{}^4T_1\rangle = \cos\phi|{}^4T_1(e^2t_{2g}^2)\rangle + \sin\phi|{}^4T_1(e^3t_{2g}^4)\rangle \quad (4)$$

the octahedral crystal field ( $10D_q$ ) and the intraatomic Coulomb interactions ( $B$ , Racah) such that  $\cos\phi = 1$  in a strong field, while  $\cos\phi = 2/\sqrt{5}$  and  $\sin\phi = -1/\sqrt{5}$  in a weak field. The effective spin–orbit coupling constant  $\nu$  of the  $\text{Co}^{\text{II}}$  ion is a function of the mixing coefficients and the one-electron spin–orbit coupling constant  $\zeta$  ( $\approx 540 \text{ cm}^{-1}$  for the free ion) [Eq. (5a)],

$$\nu = -(\frac{1}{3})\gamma\zeta \quad (5a)$$

where

$$\gamma = (\frac{1}{2})[\sin^2\phi - 2\cos^2\phi + 4\sin\phi\cos\phi] \quad (5b)$$

The value of  $-\gamma$  increases from 1 to  $3/2$  in passing from the strong-field to the weak-field limit. The second term in Equation (3) describes the splitting of the  ${}^4T_1$  orbital ground state of the  $\text{Co}^{\text{II}}$  ion by trigonal distortion, with the  $C_3$  axis of **3** defining the  $z$  direction.

In order to keep the number of states and unknowns manageable, the effects of spin–orbit coupling on the state energies of the  $\text{Co}^{\text{III}}$  ions are described by the usual bilinear spin Hamiltonian (3rd term), and it is assumed that the local symmetry of the **1a** moieties is axial as in the monomeric species (i.e., the rhombicity parameter  $E$  is taken to be zero). The main principal axes  $z'$ ,  $z''$ , and  $z'''$  of the zero-field operators are interchangeable by  $C_3$  symmetry and make an angle  $\alpha'$  with the threefold axis of the molecule, which is not necessarily identical to the molecular structure based angle  $\alpha$ ; we will make the reasonable assumption that these angles are essentially equal (see below). The exchange interactions between the Co ions are described by the fourth term. Unquenched orbital contributions to the angular momenta of the ions may lead to anisotropic exchange, which is represented in Equation (3) by nonisotropic  $J_i$  tensors.<sup>[11]</sup> The Zeeman term for  $\text{Co}^{\text{II}}$  comprises explicitly the magnetic interactions of both spin and orbital momenta whereas, at  $\text{Co}^{\text{III}}$ , the latter interaction is only implicitly accounted for by adopting  $g$  values different from 2 (5th term). The orbital Zeeman term depends, like the spin–orbit coupling, on the coefficient  $\gamma$ . The  $J_i$  and  $g_i$  tensors are assumed to be diagonal,  $(x_\perp, x_\perp, x_\parallel)$ ,  $x = J$  or  $g$ , in the principal axes of the local zero-field tensors, with the axial components,  $J_\parallel$  and  $g_\parallel$ , corresponding to the  $z'$ ,  $z''$ , and  $z'''$  directions, that is, the principal axes of the  $D_i$ ,  $J_i$ , and  $g_i$  tensors at each site ( $i = 1, 2, 3$ ) are assumed to be colinear.

We study the magnetic properties of the Hamiltonian [Eq. (3)] by means of the following procedure. The Hamiltonian matrix is constructed in the product representation spanned by the 324 basis states  $|l = 1, m\rangle|s_4 = 3/2, m_4\rangle|s_1 = 1, m_1\rangle|s_2 = 1, m_2\rangle|s_3 = 1, m_3\rangle$ . The magnetic quantum numbers  $m$  refer to the quantization axis  $z$ . Diagonalization of the Hamiltonian matrix was accomplished numerically. The powder averaging is achieved by performing a single calculation in which the magnetic field is chosen as  $H_x = H_y = H_z = H/\sqrt{3}$ , where  $H$  is the applied magnetic field. The molar powder susceptibility at temperature  $T$  ( $\chi_{\text{av}} = (\chi_x + \chi_y + \chi_z)/3$ ) is computed from the eigenpairs  $W_i$  and  $|\Psi_i\rangle$ , by using expression (6), where  $Z$  is the partition function,

$$\chi_{\text{av}} = -\frac{\mu_B N}{HZ\sqrt{3}} \sum_{i=1}^{324} \sum_{\alpha=x,y,z} \langle \Psi_i | [\gamma] + 2\vec{s}_4 + \sum_{j=1,2,3} \hat{g}_j \cdot \vec{s}_j | \Psi_i \rangle e^{-W_i/kT} \quad (6)$$

$N$  the Avogadro number, and  $x$ ,  $y$ , and  $z$  are labels for the principal axes of the susceptibility tensor. The calculated susceptibility is converted into the effective magnetic moment by the

standard expression  $\mu_{\text{eff,theo}}/\mu_B = [3k\chi_{\text{av}}T/N\mu_B^2]^{1/2}$ , where  $k$  is the Boltzmann constant. The  $\mu_{\text{eff}}$  data of  $[\text{PPh}_4]\mathbf{3}$ , recorded at the temperatures  $T_i$  in the range 5–350 K in a field of 0.1 T (Fig. 11), are fitted with the theoretical model by simplex minimization<sup>[40]</sup> of the quantity  $R$  [Eq. (7)].

$$R = \frac{\sum_{i=1}^n [\mu_{\text{eff,exp}}(T_i) - \mu_{\text{eff,theo}}(T_i)]^2}{\sum_{i=1}^n [\mu_{\text{eff,exp}}(T_i)]^2} \quad (7)$$

The molecular  $g$  factors, needed for comparison with the EPR results, are evaluated from the resonance condition  $g_{p,\text{tet}} = \Delta E/(\mu_B H_p)$  ( $p = \parallel, \perp$ ), where  $\Delta E$  is the magnetic splitting of the lowest Kramers doublet calculated with the Hamiltonian [Eq. (3)] in a field parallel or perpendicular to the  $z$  axis. We note that the spin Hamiltonian [Eq. (3)] is a generalization of the Hamiltonian used by Abragam and Pryce<sup>[38, 39]</sup> to interpret the  $g$  values of monomeric  $\text{Co}^{\text{II}}$  compounds.

**Analysis of the EPR and magnetic data:** The effective Hamiltonian [Eq. (3)] depends on eight parameters ( $\alpha'$ ,  $\nu$ ,  $\delta$ ,  $D$ ,  $J_\parallel$ ,  $J_\perp$ ,  $g_\parallel$ , and  $g_\perp$ ); the concern of overparameterization in the analysis procedure therefore arises. A global shift of the  $\mu_{\text{eff}}$  vs.  $T$  curve can be brought about in a variety of ways, for example, by changing the value of either the  $J$  or the  $g$  factors. The shape of the  $\mu_{\text{eff}}$  vs.  $T$  curve, notably the height of the hump at 40 K relative to the high-temperature tail, can be modulated by variations in the anisotropy of both the  $J$  and the  $g$  values. Furthermore, the magnetic data are not only characterized by the electronic parameters, but depend also on the structural features of the composite system. Figure 11 reveals that the choice of the angle  $\alpha'$  affects the shape of the theoretical  $\mu_{\text{eff}}$  vs.  $T$  plots. Altogether, it is not surprising that equally good fits can be obtained for different sets of parameter values (Table 1). In order to find the most appropriate solution, other selection criteria need to be considered in addition to minimization of  $R$ . The criteria we consider important are the following:

- The  $g_\parallel$  and  $g_\perp$  values of **3**, defined by the resonance condition  $g_{p,\text{tet}} = \Delta E/(\mu_B H_p)$  in which  $\Delta E$  is the magnetic splitting of the lowest Kramers doublet of the Hamiltonian [Eq. (3)], should closely match the EPR data for these quantities.
- The calculated  $D_{\text{tet}}$  value, defined as half the energy gap separating the ground and first excited Kramers doublets, should be considered in the context of the temperature-dependence of the intensity of the EPR resonance.
- Considering that the structures of the free and coordinated **1a** are very similar, the deviation between the monomeric and tetrameric values for the intrinsic parameters— $g_\parallel$ ,  $g_\perp$ , and  $D$ —of the  $\text{Co}^{\text{III}}$  sites should remain within reasonable boundaries.
- The spin–orbit coupling parameter must lie within the strong- and weak-field limits of  $180 \leq \nu \leq 270 \text{ cm}^{-1}$ .
- By reason of the axial nature of the  $\text{Co}^{\text{III}}$  sites, it is to be expected that the principal axes of the  $J_i$ ,  $g_i$ , and  $D_i$  tensors at each **1a** moiety are collinear and that the main principal axes ( $z'$ ,  $z''$ , and  $z'''$ ) are orthogonal to the **1a** planes as indicated in Figure 6, that is,  $\alpha \approx \alpha'$ .

The target data are summarized in the first line of Table 1.

Taking the above mentioned points into account, the best fits are found for  $\delta \approx 500\text{--}1000 \text{ cm}^{-1}$  (Table 1). In this range, the optimized  $g_{\parallel,\text{tet}}$  values are close to the target number, whereas  $g_{\perp,\text{tet}}$  is on the low side. The values for  $g_{\parallel,\text{tet}}$  and  $g_{\perp,\text{tet}}$  converge to a common value on lowering  $\delta$ , and the  $g_{\text{tet}}$  tensor becomes isotropic for  $\delta \approx 0$  (see Table 1). The isotropy is a consequence

Table 1. Spin-Hamiltonian parameters obtained by least-squares fitting of the magnetic susceptibility data of [PPh<sub>4</sub>]3 recorded at 0.1 T. Optimized values of adjustable parameters in Equation (3) are given with decimal point; remaining parameters are kept constant during fitting [a].

	$\delta/\text{cm}^{-1}$	$D/\text{cm}^{-1}$	$J/\text{cm}^{-1}$ [b]	$g_{\parallel}$	$g_{\perp}$	$g_{\parallel,\text{tet}}$	$g_{\perp,\text{tet}}$	$D_{\text{tet}}/\text{cm}^{-1}$ [c]	$R \times 10^5$
1		37 [d]		2.65 [d]	2.02 [d]	2.95 [e]	9.65 [e]	12.5 [e]	0
2	2000	35.4	-17.6	4.2	2.0	2.8 [f]	8.7 [f]	8.9 [f]	3.0
3	1000	34.9	-19.4	3.8	2.0	2.7	9.0	9.6	1.5
4	500	34.3	-23.5	3.6	2.0	2.9	9.0	9.1	1.6
5	250	34.5	-25.8	3.3	2.1	3.7	8.8	9.2	2.5
6	0	32.9	-26.9	3.3	2.1	7.3	7.2	9.2	4.2
7	-1000	38.8	-26.5	4.1	1.6	16.3	1.0	17.0	17.4

[a]  $\nu = -\gamma\zeta/3$ ,  $-\gamma = 5/4$  for all entries,  $\zeta = 540 \text{ cm}^{-1}$ . The angle  $\alpha'$  is set at  $55^\circ$ . [b]  $J = J_{\perp} = J_{\parallel}$ . [c] Defined as half the energy gap between the ground and first excited Kramers doublets of Equation (3). [d] Obtained from magnetic susceptibility of monomer. [e] Obtained from EPR data of tetramer. [f] Calculated in the ground Kramers doublet of Equation (3), using spin-Hamiltonian parameters given in the same line.

of the increase in symmetry of the spin Hamiltonian to cubic for  $\delta = 0$  and  $\alpha' = \arccos(1/\sqrt{3})$ . This behavior serves as a positive check for the calculation routine employed. At this, the magic angle, the main principal axes ( $z'$ ,  $z''$ , and  $z'''$ ) of the  $J_i$ ,  $g_i$ , and  $D_i$  tensors ( $i=1, 2, 3$ ) are orthogonal as required for cubic symmetry (Fig. 6). The deterioration of the  $R$  values and the reversed order of the  $g_{\text{tet}}$  factors computed for  $\delta < 0$  (line 7, Table 1,  $g_{\parallel,\text{tet}} > g_{\perp,\text{tet}}$ ) require that  $\delta > 0$  for obtaining acceptable solutions. Hence, in the framework of the Hamiltonian [Eq. (3)], the observed anisotropy of  $g_{\text{tet}}$  can only arise from a trigonal distortion of positive sign ( $\delta > 0$ ), stabilizing a singlet orbital ground state,  $^4A_2$ , at the Co<sup>II</sup> ion. The calculated  $g_{\parallel}$  and  $g_{\perp}$  values for both the Co<sup>II</sup> monomer and the studied tetramer invert in magnitude as  $\delta$  is varied from positive to negative; this provides good support for the conclusion that  $\delta$  is positive for the Co<sup>II</sup> in the tetramer.

The  $D_{\text{tet}}$  values lie in a narrow range 9–11  $\text{cm}^{-1}$ , slightly below the EPR value estimated for this quantity from the overly simple Equation (2). The optimized values for the intrinsic zero-field parameter of the Co<sup>III</sup> ions in the tetramer ( $D \approx 33\text{--}38 \text{ cm}^{-1}$ ) closely match the number deduced from the magnetic data for the monomeric Co<sup>III</sup> species. Furthermore, Table 1 shows that the values for the Co<sup>III</sup> monomeric and tetrameric values for  $g_{\perp}$  almost match. However, the  $g_{\parallel}$  values of the tetramer are on the high side of the monomeric value, and we consider this the most troubling feature of our model. Different causes for the discrepancy in the  $g_{\parallel}$  values can be considered: i) distortions of the 1a ions in the assembly of the tetranuclear ion, ii) neglect of the temperature-independent paramagnetism of the Co<sup>III</sup> sites in the treatment of the tetramer, iii) neglect of anisotropic exchange, and iv) limitations of the spin Hamiltonian [Eq. (3)] in describing the magnetic properties of the molecule. The results of fits performed at the limits of the allowed range for the effective spin-orbit coupling constant show that the optimized parameter values do not significantly differ from the numbers found in the middle of the range. Finally, the exchange-coupling constants  $J$  obtained have a ferromagnetic sign and lie in the range  $-22 \pm 5 \text{ cm}^{-1}$ .

We now return to discuss the calculation of the temperature-dependence of the EPR intensity employing the optimal set of spin-Hamiltonian parameters deduced from variable-temperature magnetic susceptibility data of the tetranuclear compound. The agreement with the experimental data is far from ideal (see Curve B in Fig. 10). In order to analyze the discrepancy, we present a number of energy-level diagrams (Fig. 12):

a) Diagram a shows the zero-field splittings in octahedral symmetry, that is, calculated with  $\delta = 0$  and  $\alpha' = \arccos(1/\sqrt{3})$ . The levels appear as doublets ( $E'$  and  $E''$ ) and quartets ( $U'$ ), where the symmetry labels refer to irreducible representations of the double group  $O^*$ .

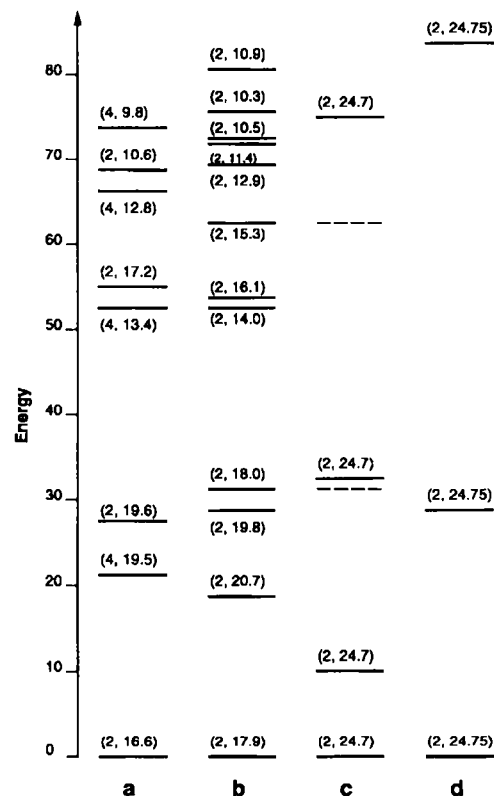


Fig. 12. Energy level diagrams ( $\text{cm}^{-1}$ ) showing the eigenvalues of the Hamiltonian [Eq. (3)] (Diag. a, b, and c) and of the axial zero-field Hamiltonian [Eq. (3)] (Diag. d). Values used:  $\delta = 0$ ,  $J = -23.5 \text{ cm}^{-1}$  (Diag. a);  $\delta = 500 \text{ cm}^{-1}$ ,  $J = -23.5 \text{ cm}^{-1}$  (Diag. b);  $\delta = 500 \text{ cm}^{-1}$ ,  $J = -500 \text{ cm}^{-1}$  (Diag. c); the remaining parameters are taken as  $\nu = 225 \text{ cm}^{-1}$ ,  $D = 34.3 \text{ cm}^{-1}$ ,  $\alpha' = \arccos(1/\sqrt{3})$ ,  $D_{\text{tet}} = 14.2 \text{ cm}^{-1}$  (Diag. d). Degeneracy and expectation value,  $\langle S^2 \rangle$ , of the states are indicated in parentheses. Diagram a is obtained in  $O_h$  symmetry, and Diagrams b, c, and d in  $D_3$  symmetry. The broken lines in Diagram c indicate the energy eigenvalues of the Hamiltonian [Eq. (1)] as obtained in the states  $|^9/2; M\rangle$ ,  $M = \pm 9/2$  and  $\pm 7/2$ , using a value of  $D_{\text{tet}}$  that is equal to half the splitting between the ground and first excited state. The ground-state energies are taken as the zero point of the energy scale.

b) Diagram b shows a trigonal distortion induced by crystal-field splitting ( $\delta \neq 0$ ), which removes the degeneracies of the  $U'$  states; this results in a level scheme consisting of single Kramers doublets. The parameter values used in the calculation of Diagram b are obtained from a fit of the magnetic susceptibility data (line 4, Table 1). Figure 12 also presents the expectation values of the square of the total spin operator,  $\langle \hat{S}^2 \rangle$ , evaluated in the states indicated. The expectation values deviate significantly from the values for the pure spin numbers,  $S(S+1)$  (where  $S = 9/2, 7/2, \dots$ ), in the cases of

weak exchange (Diag. a,b) and indicate strong spin-state mixing induced by the  $v$  and  $D$  terms in the Hamiltonian.

- c) Diagram c presents the energy levels calculated by setting  $|J| \gg D$ . The exchange interactions give rise to large energy separations between the almost pure spin multiplets, which are far too few in number at low energy to fit the steep decay of the EPR intensity at  $T > 14$  K (Fig. 10). This indicates that  $J$  cannot be much larger than the determined value.
- d) Diagram d depicts the relative energies of the zero-field splitting Hamiltonian [Eq. (3)] adopting for  $D_{\text{eff}}$  the value obtained from fitting of the variable-temperature EPR data [Eq. (2)].

A comparison of the Diagrams a, b, and d reveals that the density of states in Diagram d is unrealistically low. The density of states has an important impact on the temperature-dependence of the EPR intensity, owing to depopulation of the resonant ground doublet with temperature. As can be seen from Curve B in Figure 10, the temperature variation of the EPR intensity calculated on the basis of the crowded level scheme (Diag. b) parallels the steep decay observed in the experimental data more closely than does Curve A obtained for the sparse level scheme (Diag. d). However, the temperature range with constant intensity ( $T < 8$  K) obtained with Diagram b is narrower than that observed ( $T < 13$  K); this suggests that the energy gap between the ground state and first excited state, evaluated with the optimal parameters given in Table 1, is smaller than the actual splitting. The lack of agreement is somewhat mitigated if one takes into consideration that the Hamiltonian [Eq. (3)] describes the energies of 324 states on the basis of only five independent parameters:  $\delta$ ,  $D$ ,  $J$ ,  $g_{\parallel}$ , and  $g_{\perp}$  ( $\gamma$  is fixed as described). Thus, it is to be expected that a fit of the magnetic susceptibility data will be insensitive to individual splittings because it requires a global agreement with experiment over a broad temperature range. A simple model for the temperature-dependence of the EPR intensity, accounting for a high density of states, is given by Equation (8), where  $E_1$  is the energy of the first excited state

$$I_1 T = c / (1 + e^{-E_1/kT} + 10e^{-E_2/kT}) \quad (8)$$

and  $E_2$  the energy of an effective, 10-fold degenerate state representing the next ten excited levels (Diag. b). As can be seen from Curve C of Figure 10, good agreement with experiment is found for  $E_1 = 35$  and  $E_2 = 60 \text{ cm}^{-1}$ . This result suggests that the energy gap between the ground state and the first excited state is about twice as large as the splitting calculated from the susceptibility data. The EPR and the magnetic analyses agree in the fact that the number of low-lying states needs to be larger than in Diagram d in order to interpret the data.

**Discussion of spin-Hamiltonian parameters:** The ferromagnetic exchange interaction observed in **3** raises questions concerning the underlying coupling mechanism. As the  $\text{Co}^{\text{III}}$  and  $\text{Co}^{\text{II}}$  ions are separated by 3 Å, the exchange coupling is expected to be ligand-mediated. Strong superexchange pathways require considerable overlap among magnetic orbitals on neighboring ions. We have seen that by far the strongest interaction between the  $\text{Co}^{\text{III}}$  ions and the bridging oxygen donors is with the  $\text{Co}^{\text{III}}$   $B_1$  orbital; in principle, this orbital is best able to participate in ligand-mediated exchange coupling. However, as noted above, the  $\text{Co}^{\text{III}}$   $B_1$  orbital is high in energy and empty. We suggest this ligand-determined bonding effect eliminates antiferromagnetic exchange in **3**, while leaving open the possibility of ligand-medi-

ated enhancement of ferromagnetic coupling by a Goodenough–Kanamori process.

If this analysis is correct, the electronic structure of any magnetic ion  $M_n$  that is not a  $d^9$  ion also should be distorted by  $[\kappa^4\text{-PAC*}]^{4-}$  to eliminate strong antiferromagnetic superexchange with any second metal  $M_n$  in the contiguous site, providing that  $[\kappa^4\text{-PAC*}]^{4-}$  is bound in a planar configuration and that any additional axial ligands are not also very strong  $\sigma$  donors. Therefore, dominant ferromagnetic exchange might become a general property for these systems. It is of interest to note that, not only can the  $B_1$  orbital be isolated in energy by using  $[\kappa^4\text{-PAC*}]^{4-}$ , but our experience with a family of related ligands shows that the metal  $B_1$  energy can be tuned over a considerable energy range by manipulation of the peripheral structure of the ligand.<sup>[21]</sup> This opens the possibility of adjusting the  $B_1$  orbital energy to maximize the ferromagnetic exchange interaction through ligand design, while leaving the structural features of the bridging network minimally disturbed.

The expression given by Goodenough<sup>[20]</sup> for the ferromagnetic exchange-coupling constant  $J_F$ , derived from the interaction between a half-filled orbital and an empty orbital centered at two interacting paramagnetic sites, essentially reads  $J_F \approx -\beta^2 J_{\text{intra}}/U^2$  (not including the local spin factors). The parameters figuring in this expression are the interionic transfer integral  $\beta$ , connecting the half-filled orbital and the empty orbital, an intraatomic exchange integral  $J_{\text{intra}}$ , and the energy needed for transferring the electron  $U$ . In the  $\text{Co}^{\text{II}}\text{--Co}^{\text{III}}$  moieties of the molecule,  $U$  is expected to depend linearly on the energy of the  $B_1$  level at the  $\text{Co}^{\text{III}}$  site, according to  $U = c + E(B_1)$ . Consequently, ligand-induced changes in  $E(B_1)$  will modify the magnitude of  $J_F$ . The strongest ferromagnetic interactions should arise for  $B_1$  level energies just above the pairing limit, below which the Goodenough mechanism would break down as the ground-state spin of  $\text{Co}^{\text{III}}$  would become high. Alternatively, stabilization of the  $B_1$  orbital might convert the  $\text{Co}^{\text{III}}$  to a more conventional, strong axial Lewis acid such that it would bind additional ligands and become a typical low spin  $\text{Co}^{\text{III}}$  ion. However, it should be borne in mind that predictions for the value of  $J_F$  based on ligand control of  $U$  may be blurred by changes in  $\beta$  produced by the ligand modifications. These considerations suggest many novel investigations.

As noted above, the structural as well as the magnetic data of the tetranuclear compound reveal a trigonal distortion in the octahedral coordination sphere of the central  $\text{Co}^{\text{II}}$  ion, that is, the O– $\text{Co}^{\text{II}}$ –O angles ( $71^\circ$ ) are distorted from the octahedral value ( $90^\circ$ ), and the distortion parameter  $\delta$ , occurring in the spin Hamiltonian [Eq. (3)], is found to be positive. The angle  $\theta$  between the  $C_3$  axis and the  $\text{Co}^{\text{II}}\text{--O}$  bonds is  $60^\circ$ , that is,  $5.3^\circ$  greater than the value pertaining to octahedral symmetry. A detailed crystal-field analysis of the relation between  $\delta$  and  $\theta$  has been given by Gerloch and Qusted.<sup>[133]</sup> The study shows that the  $\theta$ -dependence of both the magnitude and sign of  $\delta$  may drastically change depending on the value adopted for the second-order crystal-field radial parameter,  $C_p$ . Gerloch and Qusted concluded from single-crystal studies of the magnetic properties in a series of monomeric  $\text{Co}^{\text{II}}$  compounds with slightly “squashed” octahedral coordination ( $\theta \geq 54.7^\circ$ ) that the orbital ground state of the  $\text{Co}^{\text{II}}$  ion is doubly degenerate ( $\delta < 0$ ) in these systems. With the same crystal-field parameters suggested by these authors, notably a large value for  $C_p$ , the theoretical relationship between  $\delta$  and  $\theta$  also would predict a negative  $\delta$  value at the  $\text{Co}^{\text{II}}$  center of the tetranuclear system. However, the present study reveals that in the tetranuclear compound the

inverse relationship between  $\delta$  and  $\theta$  seems to hold, that is,  $\delta$  is clearly positive in a squashed octahedral environment. The origin of this discrepancy calls for further analysis. We suggest it might result from the weakness of the crystal field at  $\text{Co}^{\text{II}}$  in the tetranuclear complex **3**.

## Conclusion

In this report, we have described the synthesis, characterization, and magnetic properties of the salt  $[\text{PPh}_4]\text{3}$ . The system exhibits moderate intramolecular ferromagnetic exchange coupling. Analysis of the magnetic properties leads us to suggest a ligand-based approach for controlling exchange pathways. Planar strongly  $\sigma$ -donating chelates of the  $[\kappa^4\text{-PAC}^*]^{4-}$ -type isolate at high energy one d orbital of any metal ion coordinated in the tetradentate site; for any ion other than a  $d^9$  ion, this d orbital will be empty and is likely to be the most important d orbital for superexchange interactions with a second metal ion coordinated at the bidentate alkoxide donor site. It is unavailable for antiferromagnetic exchange coupling, but it can enhance ferromagnetic exchange coupling by overlap with a magnetic orbital of the metal in the bidentate site.

Importantly, if the analysis is correct, the observed ferromagnetic exchange coupling in **3** would owe its origin to the underlying bonding properties of  $[\kappa^4\text{-PAC}^*]^{4-}$  to just the  $\text{Co}^{\text{III}}$  ions. The geometry and electronic structure are imposed by the  $[\kappa^4\text{-PAC}^*]^{4-}$  ligand on the  $\text{Co}^{\text{III}}$  ion and on other metal ions in oxidation states for which the square-planar geometry is rarely if ever observed. But the design approach might not be limited to planar tetradentate  $M_n$  ions: the isolation at high energy of the important orbital for superexchange is achieved with strongly  $\sigma$ -donating  $[\kappa^4\text{-PAC}^*]^{4-}$ -type complexes when axial ligands are also present giving five- and six-coordinate geometries.<sup>[21]</sup> The suggested approach might help to expand practical thinking about the control of exchange coupling to include the bonding properties of total chelating ligand complements as control elements. This is also appealing because one has to think only about the bonding at a single metal ion of an interacting pair or group to conceive of controlling the exchange interactions. It is important to recognize that studies of related systems should be undertaken to further test the proposed approach.<sup>[41]</sup>

## Experimental Procedure

**Materials and methods:** All solvents and reagents were reagent grade and were used as received. Infrared spectra were obtained on a Mattson Galaxy Series 5000 FTIR spectrometer. UV/Vis spectra were obtained on a Perkin-Elmer Lambda Array 3840. Conventional X-Band EPR spectra were recorded in derivative mode on a Bruker ER300 spectrometer equipped with an Oxford ESR-900 helium flow cryostat. A variable-temperature study was conducted to obtain an estimate of the molecular zero-field splitting based on an  $I_s T$  vs.  $T$  plot, where  $I_s$  is the intensity calculated by double integration of the EPR signal. An internal  $S = 1/2$  standard, for which  $I_s T$  is independent of temperature, was employed to calibrate the temperature and to estimate the error in  $I_s$ . A noncoordinating  $\text{Cu}^{\text{II}}$  standard,  $[\text{Cu}(\text{TPP})]$  (TPP = 5,10,15,20-tetraphenylporphinate), was chosen to minimize disruption of the tetranuclear cobalt complex, and it was found that  $[\text{Cu}(\text{TPP})]$  does not perturb the EPR spectrum of **3** at workable concentrations. The mean value of the raw  $[\text{Cu}(\text{TPP})]$  data, taken over the temperature range considered ( $5 \leq T \leq 27$  K), defines the base line relative to which the temperature variation of the  $I_s T$  was plotted for the tetramer. A margin of error in the  $I_s T$  values, arising from inaccuracies in both the temperature measurement and the double integration procedure, was defined as the standard deviation of the distribution of the  $I_s T$  values measured around the  $[\text{Cu}(\text{TPP})]$  baseline. This same error margin was adopted for the data for compound **3**.  $^1\text{H}$  NMR spectra were measured at 300 MHz on an IBM NR/300 FT-NMR spectrometer.  $^1\text{H}$  NMR chemical shifts are reported in  $\delta$  (ppm vs.  $(\text{CH}_3)_4\text{Si}$ ) with the solvent as an internal standard. Microanalyses were performed by Midwest Microlabs.

**Magnetic susceptibility data:** The magnetic susceptibility measurements were performed on a Quantum Design SQUID MPMG at the University of Colorado at Boulder. The data were collected in the range of 5–350 K for powdered microcrystalline samples of  $[\text{PPh}_4]\text{3}$  at two measuring fields (0.1 and 1 T) and  $[\text{PPh}_4]\text{1a}$  at 0.1 T. Data for microcrystalline  $[\text{PPh}_4]\text{3}$  were also collected in frozen nujol at 0.1 T and were found not to differ from the data for the unsuspended sample. The two separate field data sets differ insignificantly and fitting procedures were focused on the 0.1 T data. Diamagnetic corrections were applied based on Pascal's constants.

**Synthesis of  $[\text{PPh}_4]\text{3}$ :** To an orange solution of  $[\text{PPh}_4]\text{1a}$  [22] (150 mg, 0.1 mmol) in  $\text{CH}_2\text{Cl}_2$  (50 mL) was added  $\text{Co}(\text{BF}_4)_2 \cdot 6\text{H}_2\text{O}$  (2 equiv, 11 mg, 0.03 mmol), and the mixture was stirred (24 h). The red solution was filtered through Celite and the  $\text{CH}_2\text{Cl}_2$  removed under vacuum. Benzene (40 mL) was added to the solid residue, and the solution evaporated slowly (60 °C, 12 h) to give red crystals: Yield 11 mg (25%, the first crop was collected at low yield to assist in attaining high purity). Larger samples were prepared for magnetic studies by scaling the procedure.  $^1\text{H}$  NMR (300 MHz,  $\text{CDCl}_3$ ):  $\delta$  = 17.5 (s, 18H), 10.7 (s, 18H), -18.9 (s, 18H), -45.6 (s, 18H). IR (Nujol):  $\nu$  [ $\text{cm}^{-1}$ ] = 1707, 1642. UV/Vis ( $\text{CH}_2\text{Cl}_2$ ):  $\lambda_{\text{max}}$  [nm] ( $\epsilon$  in  $\text{M}^{-1}\text{cm}^{-1}$ ) = 236 (3100), 316 (1600), 346 (1500), 474 (2100). Anal. calcd for  $\text{C}_{24}\text{H}_{20}\text{P}(\text{C}_{15}\text{H}_{24}\text{N}_2\text{O}_3\text{Co})_3\text{Co}$ : C, 54.80; H, 6.13; N, 5.56; P, 2.05. Found: C, 54.85; H, 6.10; N, 5.64; P, 2.31.

**Crystallographic measurements:** Single crystals of  $[\text{PPh}_4]\text{3}$  at  $20 \pm 1$  °C are orthorhombic, space group  $Pbca-D_{2h}^{13}$  (No. 61), with  $a = 20.741(4)$ ,  $b = 24.489(6)$ ,  $c = 29.340(5)$  Å,  $V = 14903(6)$  Å<sup>3</sup>, and  $Z = 8$  ( $d_{\text{calc}} = 1.348$   $\text{g cm}^{-3}$ ;  $\mu_a(\text{MoK}\alpha) = 0.96$   $\text{mm}^{-1}$ ). A total of 10286 independent reflections having  $2\theta(\text{MoK}\alpha) < 45.8^\circ$  (the equivalent of 0.6 limiting  $\text{CuK}\alpha$  spheres) were collected at room temperature on a computer-controlled autodiffractometer using full ( $1.2^\circ$ -wide)  $\omega$  scans and graphite-monochromated  $\text{MoK}\alpha$  radiation. The structure was solved by direct methods with the Nicolet SHELXTL software package as modified at Crystallogics Company. The resulting structural parameters have been refined to convergence [ $R_1$ (unweighted, based on  $F$ ) = 0.057 for 3911 independent reflections having  $2\theta(\text{MoK}\alpha) < 45.8^\circ$  and  $I > 3\sigma(I)$ ] by using counter-weighted cascade block-diagonal least-squares techniques and a structural model that incorporated anisotropic thermal parameters for all nonhydrogen atoms of the anion and for the P atom of the cation, and isotropic thermal parameters for the phenyl carbons of the cation and for all hydrogen atoms. The six carbon atoms and five hydrogen atoms for each of the four independent phenyl groups of the cation were refined as rigid groups with idealized planar geometry. Nineteen of the twenty-four methyl groups of the anion were included in the refinement as idealized  $\text{sp}^3$  rigid rotors. The five remaining methyl groups could not be satisfactorily refined as rigid rotors (presumably because of disorder in the contiguous C8–O3 groups), and were therefore included in the structure factor calculations with idealized staggered configurations. Two of the 1a ligands are disordered in the solid state with two alternate positions (54/46% for the first and 70/30% for the second ligand) for the C8–O3 group. The lower-percent positions are indicated by primes in Figure 2. Further details of the crystal structure investigation may be obtained from the Director of the Cambridge Crystallographic Data Centre, 12 Union Road, GB-Cambridge CB2 1EZ (UK), on quoting the full journal citation.

**Acknowledgements:** This work was supported by the NIH, GM 44867 (T. J. C.), and U. C. Bolder (G. T. Y.).

Received: January 16, 1995 [F 56]

- [1] W. Heitler, F. London, *Z. Phys.* **1927**, *44*, 455.
- [2] H. A. Kramers, *Physica* **1934**, *1*, 182.
- [3] J. H. Van Vleck, *The Theory of Electric and Magnetic Susceptibilities*, OUP, Oxford, **1932**.
- [4] P. W. Anderson in *Solid State Physics*, Vol. 14 (Eds.: G. T. Rado, H. Suhl), Academic Press, New York, **1963**.
- [5] P. W. Anderson in *Magnetism*, Vol. 1 (Eds.: F. Seitz, D. Turnbull), Academic Press, New York, **1963**.
- [6] J. B. Goodenough, *Phys. Rev.* **1955**, *100*, 564.
- [7] J. B. Goodenough, *Phys. Chem. Solids* **1958**, *6*, 287.
- [8] J. B. Goodenough, *Magnetism and the Chemical Bond*, Wiley, New York, **1963**.
- [9] J. Kanamori, *J. Chem. Phys. Solids* **1959**, *10*, 87.
- [10] R. L. Carlin, *Magnetochemistry*, Springer, Berlin, **1986**.
- [11] A. Bencini, D. Gatteschi, *EPR of Exchange Coupled Systems*, Springer, Berlin, **1990**.
- [12] O. Kahn, *Molecular Magnetism*, VCH, New York, **1993**.
- [13] G. van Kalker, W. W. Schmidt, R. Block, *Physica* **1979**, *97B + C*, 315.
- [14] J. J. Girerd, Y. Journaux, O. Kahn, *Chem. Phys. Lett.* **1981**, *82*, 534.
- [15] E. L. Bominaar, R. Block, *Physica* **1983**, *121B + C*, 109.
- [16] P. J. Hay, J. C. Thibeault, R. J. Hoffmann, *J. Am. Chem. Soc.* **1975**, *97*, 4884.
- [17] Magnetic orbitals house the unpaired electrons—Ref. [12]. They are composed of metal orbitals on an individual paramagnetic ion and ligand orbital components that prescribe how the unpaired spins are delocalized over the diamagnetic host. The magnetic orbitals are assumed to be orthogonal on individual sites, but each pairwise relationship among the different sites may be either orthogonal or nonorthogonal. In this manner, the indirect or ligand-mediated ex-

- change is converted into a direct interaction for evaluation of the exchange-coupling constant. When at least one site in a pair of interacting paramagnetic ions has more than one unpaired electron, the total exchange interaction is the sum of the intersite exchange contributions over all the individual electron–electron pairs. Therefore, the total exchange-coupling constant generally includes contributions of opposite sign.
- [18] W. E. Hatfield, *ACS Symp. Ser.* **1974**, 5, 108, "Superexchange Interactions in Copper(II) Complexes".
- [19] R. D. Willett, D. Gatteschi, O. Kahn, *Magneto-Structural Correlations in Exchange Coupled Systems*, 140. Reidel, Dordrecht, **1985**.
- [20] Ref. [8]; p. 167.
- [21] T. J. Collins, *Acc. Chem. Res.* **1994**, 27, 279.
- [22] J. C. Brewer, T. J. Collins, M. R. Smith, B. D. Santarsiero, *J. Am. Chem. Soc.* **1988**, 110, 423.
- [23] D. W. Margerum, *Pure Appl. Chem.* **1983**, 55, 23.
- [24] J. March, *Advanced Organic Chemistry*, Wiley, New York, **1985**.
- [25] F. C. Anson, T. J. Collins, T. G. Richmond, B. D. Santarsiero, J. E. Toth, B. G. R. T. Treco, *J. Am. Chem. Soc.* **1987**, 109, 2974.
- [26] T. J. Collins, T. R. Nichols, E. S. Uffelman, *J. Am. Chem. Soc.* **1991**, 113, 4708.
- [27] K. L. Kostka, B. G. Fox, M. P. Hendrich, T. J. Collins, C. E. F. Rickard, L. J. Wright, E. Münck, *J. Am. Chem. Soc.* **1993**, 115, 6746.
- [28] Recognize that  $[\text{Co}^{\text{III}}(\kappa^4\text{-PAC}^*)]^-$  has  $C_{2v}$  symmetry such that the  $z$  axis, which lies by convention on the principal rotation axis, bisects the O–Co–O angle. Therefore, the destabilized orbital is labeled  $d_{xz}$  and not  $d_{z^2-y^2}$ , as in the  $D_{4h}$  symmetry.
- [29] T. J. Collins, T. G. Richmond, B. D. Santarsiero, B. G. R. T. Treco, *J. Am. Chem. Soc.* **1986**, 108, 2088.
- [30] T. J. Collins, E. S. Uffelman, *Angew. Chem. Int. Ed. Engl.* **1990**, 28, 1509.
- [31] T. J. Collins, J. M. Workman, *Acta Crystallogr.*, **1993**, C49, 1426–1428.
- [32] T. J. Collins, R. D. Powell, C. Slebodnick, E. S. Uffelman, *J. Am. Chem. Soc.* **1991**, 113, 8419.
- [33] M. Gerloch, P. N. Quedstedt, *J. Chem. Soc. (A)* **1971**, 3729.
- [34] A. L. Companion, M. A. Komarynsky, *J. Chem. Educ.* **1964**, 41, 257.
- [35] We believe that it is of some consequence to the design of solids to realize that the barriers to adjustment of  $\alpha$  within sterically allowed values will probably be small for central ions such as high-spin  $\text{Mn}^{\text{II}}$  and  $\text{Fe}^{\text{III}}$ .
- [36] R. V. Parish, *NMR, NQR, EPR, and Mössbauer Spectroscopy in Inorganic Chemistry*, Ellis Horwood, New York, **1990**.
- [37] Careful examination of the EPR spectrum suggests unresolved hyperfine interactions and a slight rhombicity as evidenced by a shoulder on the perpendicular signal. Both are neglected in the analysis.
- [38] A. Abragam, M. H. L. Pryce, *Proc. R. Soc. London* **1951**, A206, 173.
- [39] J. S. Griffith, *The Theory of Transition-Metal Ions*, Cambridge University Press, London, **1971**.
- [40] W. H. Press, B. P. Flannery, S. A. Teukolsky, W. T. Vetterling, *Numerical Recipes. The Art of Scientific Computing*, Cambridge University Press, Cambridge, **1989**, 289–293.
- [41] It would be premature to deal with the significance of other bonding features such as the  $\text{Co}^{\text{III}}\text{O}-\text{Co}^{\text{II}}$  angle, which have been shown in other systems to be of importance in determining magnetic exchange interactions; Ref. [16].